

HAO SHI^{*,**#}, HOUQUAN ZHANG^{*,**#}, LEI SONG^{*,**}, YU WU^{*,**}**VARIATION OF STRATA PRESSURE AND AXIAL BOLT LOAD AT A COAL MINE FACE UNDER THE EFFECT OF A FAULT****ZMIENNOŚĆ CIŚNIENIA GÓROTWORU I OBCIĄŻENIA OSIOWE DZIAŁAJĄCE NA SEGMENTY OBUDOWY W REJONIE PRZODKA SPOWODOWANE OBECNOŚCIĄ USKOKÓW**

The cohesion and internal friction angle were characterized as quadratic functions of strain and were assumed to follow the Mohr-Coulomb criterion after the yield of peak strength. These mechanical parameters and their variations in post-peak softening stage can be exactly ascertained through the simultaneous solution based on the data points of stress-strain curves of triaxial compression tests. Taking the influence of the fault into account, the variation of strata pressure and roadway convergence with coal advancement, the temporal and spatial distribution of axial bolt load were numerically simulated by FLAC^{3D} (Fast Lagrangian Analysis of Continua) using the ascertained post-peak mechanical parameters according to the cohesion weakening and friction strengthening model. The change mechanism of axial load of single rock bolt as abutment pressure changes was analyzed, through the comparison analysis with the results of axial bolt load by field measurements at a coal mine face. The research results show that the simulated results such as the period of main roof weighting, temporal and spatial distribution of axial bolt load are in accordance with field measurement results, so the validity of the numerical model is testified. In front of the working face, the front abutment pressure increases first and then decreases, finally tends to be stable. A corresponding correlation exists between the variation of axial bolt load and rock deformation along the bolt body. When encountered by a fault, the maximum abutment pressure, the influential range of mining disturbance and the roadway convergence between roof and floor before the working face are all increased. In the roadways along the gob, axial bolt loads on the side of the working face decrease, while the other side one increases after the collapse of the roof. As superficial surrounding rock mass is damaged, the anchoring force of rock bolts will transfer to inner rock mass for balancing the tensile load of the bolts.

Keywords: FLAC^{3D} numerical simulation; Axial bolt load; Strata behavior; Mining and Fault effect; Strain-softening model

* STATE KEY LABORATORY FOR GEOMECHANICS AND DEEP UNDERGROUND ENGINEERING, CHINA UNIVERSITY OF MINING AND TECHNOLOGY, XUZHOU, JIANGSU 221116, CHINA

** SCHOOL OF MECHANICS AND CIVIL ENGINEERING, CHINA UNIVERSITY OF MINING AND TECHNOLOGY, JIANGSU 221116, CHINA

Corresponding author: 1990944858@qq.com; 52zhq@163.com

Zwięzłość skał oraz kąt tarcia wewnętrzznego zdefiniowano jako kwadratowe funkcje naprężenia, następnie przyjęto że ich rozkład po osiągnięciu naprężenia granicznego opisany jest wzorem Mohra-Coulomba. Wymienione parametry mechaniczne i ich zmienność po osiągnięciu naprężenia granicznego obliczyć można dokładnie poprzez jednoczesne rozwiązanie oparte o analizę punktów na krzywej wykresu rozciągania uzyskanych w testach ściskania trójosiowego. Uwzględniając wpływ obecności uskoku, zmienność ciśnienia w górotworze i konwergencji chodnika wraz z postępem przodka, rozkłady naprężeń i obciążeń działających na segmenty obudowy i ich zmienność w czasie i przestrzeni modelowano w oparciu o pakiet FLAC^{3D} (Fast Lagrangian Analysis of Continua), wykorzystując uprzednio obliczone wielkości parametrów mechanicznych dla stanu po osiągnięciu naprężenia granicznego, zgodnie z modelem słabnącej zwięzłości i wzmocnionego tarcia. Mechanizm zmiany naprężeń osiowych działających na pojedynczy segment obudowy analizowano w odniesieniu do ciśnienia warstw sąsiadujących, poprzez analizę porównawczą wyników pomiarów obciążeń segmentów obudowy w rejonie przodka. Wykazano, że wyniki symulacji: okresy obciążenia stropu, rozkłady naprężeń i obciążeń działających na elementy obudowy i ich zmienność w czasie i przestrzeni zgodne są z wynikami pomiarów w miejscu, w ten sposób potwierdzając wiarygodność modelu numerycznego. W rejonie przodka ciśnienie warstw sąsiadujących w górotworze najpierw rośnie, następnie maleje, a w końcu stabilizuje się. Istnieje odpowiednia korelacja pomiędzy zmiennością rozkładu naprężeń i obciążeń działających na elementy obudowy a odkształceniem warstw skalnym wzdłuż konstrukcji obudowy. W przypadku wystąpienia uskoku, występuje maksymalne ciśnienie warstw otaczających- poważny czynnik powodujący wszelkiego rodzaju zaburzenia a także nasilenie konwergencji chodnika pomiędzy stropem a podłożem w rejonie przed przodkiem. W chodnikach wzdłuż zrobów, obciążenia osiowe obudowy działające z jednej strony maleją, po drugiej zaś stronie rejonu przodkowego rosną po zawale stropu. Płytką warstwa otaczającego górotworu ulega zniszczeniu, siła podtrzymująca obudowę przeniesiona zostanie wewnątrz górotworu, tak by zrównoważyć naprężenia rozciągające działające na obudowę.

Słowa kluczowe: symulacje numeryczne FLAC^{3D}, naprężenia osiowe działające na obudowę, zachowanie górotworu, górnictwo, efekt uskoku, model odprężania

1. Introduction

In deep coal mining, it is inevitable for stope roof to show strong strata pressure behavior including subsidence, caving, even rock burst, etc. under heavy mining disturbance. When encountered by a fault, the working face manifests more complex strata pressure phenomena. Therefore, it is difficult to grasp the variation of strata pressure and thus the safety of underground personnel and equipment is seriously endangered (Freidin et al., 2016; Qian et al., 2010; Rezae, 2016; Zhang et al., 2016). In coal mines of China, most of underground roadways are commonly supported by rock bolts. The working state of the bolts is affected by the geological condition and the mining factors. The change of axial bolt load in district (tail and belt) entries has a clear corresponding relationship with the distribution of abutment pressure before the working face. For two instances, the breaking of the basic roof will cause that the position of peak value of the axial bolt load in front of the working face jumps forward and the activation of the fault will cause a significant increase of the front support range of the bolts (Chen et al., 2016; He & Zhang, 2008; Tao et al., 2016). Therefore, by putting the 'sensor' function of axial bolt load into good use, the weighting of main roof and the activation of fault can be perceived in advance, and the preventive measures can be taken in time. To sum up, it is of great significance to further study the change mechanism of the axial bolt load and its exact response to the variation of the mining strata pressure, so as to ensure the safe coal production at the working face.

A lot of research work has been done (Chen et al., 2016; Su et al., 2017; Xu et al., 2015; Xu et al., 2016; Zhang et al., 2017b; Zhang et al., 2014; Zhou, 2016) on the variation of the axial bolt load and the mining pressure, by means of field measurement, numerical simulation,

laboratory experiments, etc. Chen et al. (2016) have detected the change of the axial load of bolts with the abutment pressure in front of the working face induced by mining. They found that a clear corresponding relationship existed between the change of axial bolt load and the distribution of front abutment pressure in the mining disturbance area. Through the analysis of the drastic increase or decrease of axial bolt load, Zhou (2016) found that fault activation can be reflected by the change of axial bolt load. Zhang et al. (2017b) found that the location of the peak value of axial bolt load corresponded to the junction position of broken rock and unbroken rock surrounding the roadway before the working face by a non-destructive testing method. Su et al. (2017) carried out laboratory experiments on the relationship between the deformation of rock mass and axial bolt load in the fractured zone near a fault and they found that the bearing capacity of the anchored surrounding rock has a certain reduction when the axial bolt load reaches its peak value. Xu et al. (2015) simulated the fracturing process of the key stratum overlying on the gob using RFP software and they found that the maximum abutment pressure existed in the rock mass about 10 m from the working face, the abutment pressure increased with the advance of a working face before the collapse of key stratum; when the key stratum collapsed, the abutment pressure reached the maximum value and the pressure dropped sharply and moved forward. Xu et al. (2016) simulated the coal advancing in Yangliu coal mine in Huaibei mining area by FLAC software and they found that the breaking of the roof will cause the redistribution of the abutment pressure in front of the working face.

The above research achievements are of great significance for the safety of coal mine production. A common disadvantage existed is that only one research method (like field measurement, numerical simulation, laboratory experiments, etc.) was adopted in the above investigation. By a single research means, it is not sufficient to grasp the change mechanism of the axial bolt load and its exact response to the complex variation of the mining strata pressure, especially when under the effect of a fault in this research instance. In the meantime, most of current post-peak mechanical models are based on the elastic-brittle model (Xu et al., 2015) or ideal elastic-plastic model (Xu et al., 2016). These post-peak mechanical model and rock property parameters cannot preferably reflect the mechanical behavior of strong strata pressure. In this study, a strain softening model based on Mohr-Coulomb (M-C) criterion was selected as the post-peak mechanical model after the failure of surrounding rock. The mechanical properties such as cohesion and internal friction angle, after the yielding of rock are deteriorated according to the real post-peak stress-strain curves based on the laboratory experiments. By virtue of the above two approaches, the variation of axial bolt load and strata pressure behavior under the effect of a fault may be more appropriately and preferably simulated by FLAC^{3D}. In contrast with the results of field measurements on the axial bolt load at a coal mine face, the mechanical processing of post-peak rock behavior and the numerical model built on the in-situ geological conditions can be testified for the validity. This comprehensive study in combination with field measurements and numerical simulation will significantly benefit for understanding the change mechanism of axial bolt load and the strata pressure behavior during coal advancing.

2. Project overview

The working face studied in this paper was selected at a panel of a coal mine in Huainan city, Anhui Province, China. The panel is about 1536 m long and 240 m wide in strike direction and dipping direction, respectively. The coal seam is about 3-5 m thick and its dip angle is about

3-6°. Its buried depth is about 800 m. Gas content is 4.6-5.9 m³/t and gas pressure of 1.6 MPa. The hydrogeological conditions in this mining area are simple, and the normal water inflow from the working face is 1-5 m³/h, which has less impact on the mining face. A normal fault with 30° dip angle and 4 m drop height is located at the position of 84 m before the open-off cut of the working face. The strike direction of the fault is almost perpendicular to the mining advance direction. The roof and floor rock strata and their geological descriptions are presented in the coal-rock columnar in Fig. 1.

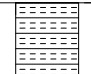
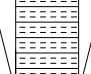



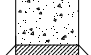
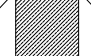
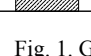
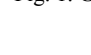
Lithology	Columnar	Rock thickness / m	Depth / m	General description
Fine sandstone		36.2	801.5	Light gray green; fracture developed; soft interlayer contained
Sandy mudstone		12.1	813.6	Gray; muddy structure; inhomogeneity; plastic
13-2 coal		2.4	816.0	Black; brittle; low strength
Mudstone 2		5.7	821.7	Ash black; soft; brittle
13-1 coal		4.3	826.0	Black; blocky; glass luster
Mudstone 1		2.2	828.2	Ash black; soft; brittle
Siltstone		3.9	832.1	Lividity; dense
Medium granit sandstone		11.5	843.6	Incanus; blocky; abundant in original fissures
Oroidovician limestone		16.7	860.3	Gray; abundant in original fissures ; plastic

Fig. 1. Geology columnar section

The fully mechanized mining and fully caving for the overall height in the gob in one time is used in this mine. Two district roadways are driven along two sides of the panel. The roadways are in rectangle with a width of 6 m and a height of 4 m. Combined anchor bolts and

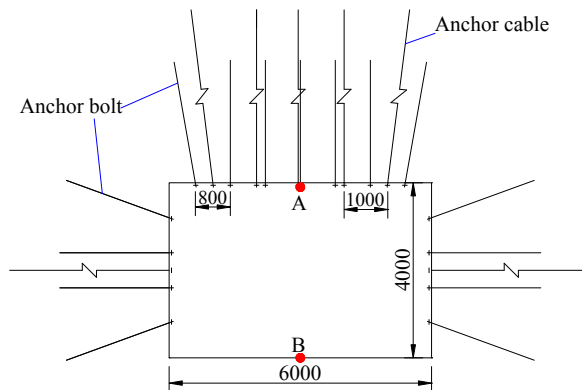


Fig. 2. Bolt support and measurement (red) points

cables were selected for the support of the roadways. The row and column spacing of the bolts are 0.8 m and 1.0 m. The lengths of roof and rib bolts are 2.8 m and 2.5 m, respectively. The row and column spacing of cables are both 1.0 m. The lengths of roof and rib cables are both 5.2 m, as shown in Fig. 2.

3. Numerical model establishment

Only some limited data can be obtained in in-situ field measurement due to the shortage of current monitoring technology and its equipment. Numerical simulation can provide more abundant visual information, which can make up for the shortage of field measurements. Therefore, in this research, based on the field measurements of axial bolt load, numerical simulation by FLAC^{3D} is adopted to systematically and deeply study the variation of strata pressure and axial bolt load of the selected working face.

The FLAC^{3D} software is developed on the basis of continuous medium mechanics. It employs an explicit Lagrangian fast algorithm to perform calculation analysis on the complex mechanical problems (Liu, 2016; Meng, 2009). It is widely used for the simulation analysis on the problem of large deformation and support design in geotechnical and mining engineering (He, 2012). Therefore, the FLAC^{3D} is feasibly chosen to simulate and analyze the real time state of axial bolt load and the strata pressure behavior.

3.1. Numerical model and its boundary condition

According to the actual project conditions of the studied working face, 240 m wide and 4 m high, a numerical model in 320 m×190 m×90 m is set up, as shown in Fig. 3. As the interaction of rock bolt with surrounding rock is the main problem focused in this study, therefore, the meshes are refined near the coal seam, as seen from the appended picture in Fig. 3. The numerical model is consisted of cuboid elements with a minimum height of about 20 cm and the number of elements is about 5.5 million. The coordinate system of the model is also established. What needs to be emphasized is that the Y-direction is consistent with the advance direction of the working face, and the zero point of the Y-direction is at the junction of the safety pillar and the working face (see Fig. 3). The advance direction of coal mining is denoted by a red arrow. Two entries are driven along the panel. A coal safety pillar 36m wide was left before the mining setup room in order to basically eliminate the influence of boundary conditions. As the long-wall mining method is used in this coal face, the roof will collapse when the working face is advanced to a certain distance. Interfaces built in FLAC^{3D} software are set at the common boundaries of coal seams and the roof/ floor. When overlying rock layers fall down on the floor, the contact surfaces of “interfaces” between roof and floor can hinder the further movement of the collapsed roof; at the same time, the load of overlying strata can be transmitted to the floor. In order to study the influence of fault, a normal fault with 30° dip angle and 4 m drop height is set at the position of about 120 m in Y-direction from the boundary according to the above in-situ conditions (see Fig. 3). The strike direction of the fault is almost perpendicular to the mining advance direction.

A uniform distributed load of 20 MPa is exerted on the top according to the buried depth of the coal seam, about 800 m. A horizontal displacement constraint around the model and a normal displacement constraint at the bottom are designed.

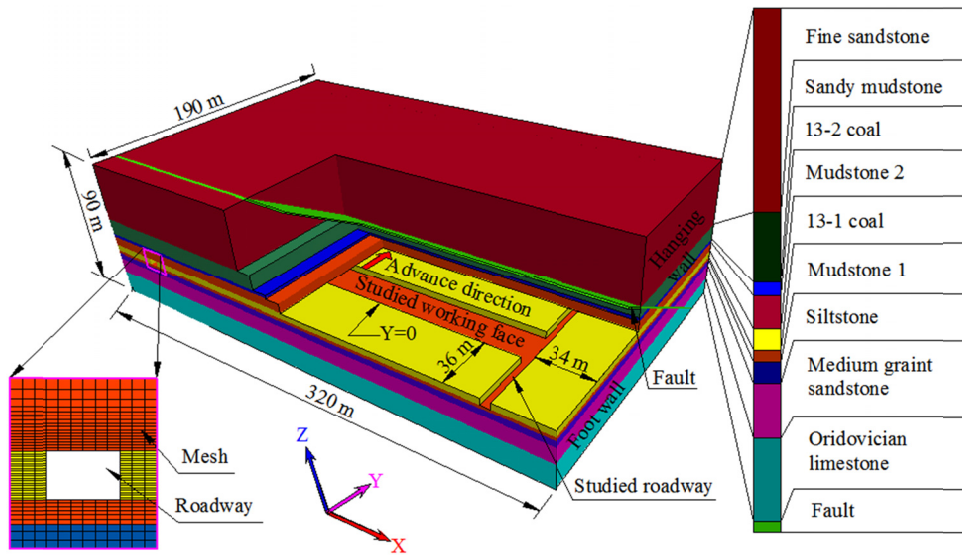


Fig. 3. Numerical model

The excavation in $FLAC^{3D}$ can be simulated by using an empty element and the advance distance was set to about 5 m based on the actual situation. After the balance of calculation at each excavation step, the data of the roof axial bolt load and the convergent displacement of the roof and floor are collected.

As the roadway support uses combined anchor bolts and cables, the structural elements built-in $FLAC^{3D}$ are used to simulate the bolts and cables and solid elements are selected for the simulation of rock strata. The interaction of the bolt and rock can be described in Fig. 4. As the shear behavior of the cable-rock interface is cohesive and frictional, a spring-slider is set at the

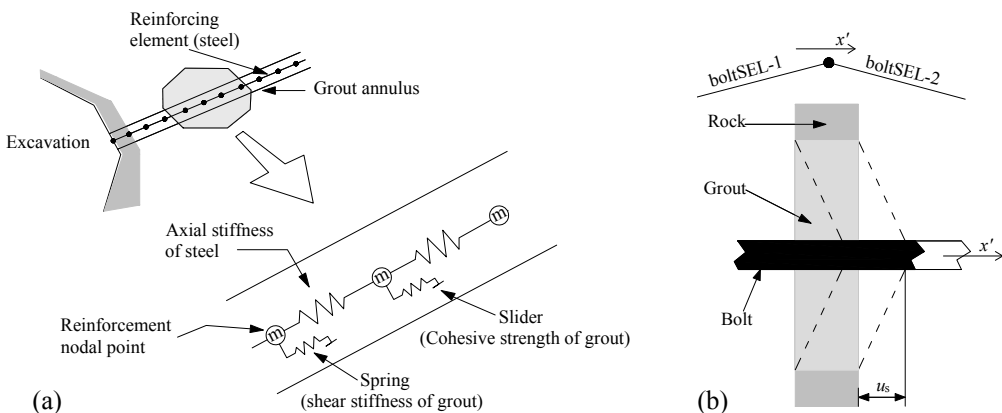


Fig. 4. Interaction of the bolt, grout and rock (Itasca Consulting Group, Inc., 2012);
 (a) Mechanical representation of a bolt, (b) Relative shear displacement between bolt and rock

nodal points, as shown in Fig. 4(a). With the increase of axial bolt load, a relative displacement (u_s , see Fig. 4(b)) would happen at the rock/grout interface and the grout/cable interface. This shear behavior of the grout annulus is described numerically by the grout shear stiffness, the grout cohesive strength etc. (Itasca Consulting Group, Inc., 2012). In addition, for the anchorage of the bolt and cable in this project, the stiffness and cohesion of the grout are set to a certain high value to simulate the anchorage section and a much higher value for the plate; the grout stiffness and cohesion corresponding to the free section is set closely to zero.

3.2. Mechanical model

In deep coal mining, large deformation and rock damage inevitably occurs in the surrounding rock of underground openings under high in situ stress and heavy mining disturbance. Before and after post-peak failure, the change of physical and mechanical parameters of surrounding rock cannot be ignored. Therefore, the strain-softening model is chosen as the constitutive model (Levent et al., 2015). This model is based on the FLAC^{3D} M-C model with nonassociated shear and associated tension flow rules. The difference lies in that the mechanical parameters such as cohesion, internal friction, etc. can harden or soften after the onset of plastic yield, as shown in Fig. 5 (where ε_1 is axial strain, ε^e is elastic strain and ε^p is plastic strain). In the M-C model, the mechanical parameters are assumed to remain unchanged after yielding; on the other hand, as for the strain-softening model, the parameters may soften or harden (Hajiabdolmajid et al., 2002; Diederichs, 2007) after yielding, although the overall strength must be reduced. Before plastic yield, it is considered that the rock only undergoes elastic strain, while after yield strength the total strain is the sum of elastic and plastic strain. The user can define the cohesion, friction as piecewise-linear functions of a hardening parameter with the plastic shear strain. It makes the mechanical properties in the model conform to the user-defined functions.

For the strain-softening model, the incremental expression of Hooke's law in terms of the principal stress and strain has the form,

$$\begin{cases} \Delta\sigma_1 = \alpha_1\Delta\varepsilon_1^e + \alpha_2(\Delta\varepsilon_2^e + \Delta\varepsilon_3^e) \\ \Delta\sigma_2 = \alpha_1\Delta\varepsilon_2^e + \alpha_2(\Delta\varepsilon_1^e + \Delta\varepsilon_3^e) \\ \Delta\sigma_3 = \alpha_1\Delta\varepsilon_3^e + \alpha_2(\Delta\varepsilon_1^e + \Delta\varepsilon_2^e) \end{cases} \quad (1)$$

where, $\Delta\varepsilon_1^e$, $\Delta\varepsilon_2^e$ and $\Delta\varepsilon_3^e$ are the incremental expressions of the principal stress strains, α_1 and α_2 are material constants defined in terms of the shear modulus G , and bulk modulus K , as the following,

$$\begin{cases} \alpha_1 = K + \frac{4}{3}G \\ \alpha_2 = K - \frac{2}{3}G \end{cases} \quad (2)$$

The shear yield function of strain-softening model has the expression as,

$$F^s = \sigma_1 - \sigma_3 N_\varphi + 2c\sqrt{N_\varphi} \quad (3)$$

where, $N_\varphi = \frac{1 + \sin \varphi}{1 - \sin \varphi}$, φ is the internal friction angle, c is the cohesion, σ_1 is the maximum principal stress, and σ_3 is the minimum principal stress.

Tensile yield strength function has the form,

$$F^t = \sigma_1 - \sigma_3 \quad (4)$$

The usual assumption is made: that total strain increments can be decomposed into elastic and plastic parts. The flow rule for plastic yielding has the form,

$$\Delta \varepsilon_i^p = \lambda \frac{\partial g}{\partial \sigma_i} \quad (5)$$

where $i = 1, 3$. λ is the coefficient of plasticity to be determined. The potential function, g , for shear yielding is g^s . This function corresponds to the nonassociated law,

$$g^s = \sigma_1 - \sigma_3 N_\psi \quad (6)$$

where, $N_\psi = \frac{1 + \sin \psi}{1 - \sin \psi}$, ψ is the dilation angle.

The potential function for tensile yielding is g^t . It corresponds to the associated flow rule,

$$g^t = -\sigma_3 \quad (7)$$

The plastic strain increments for shear failure have the form,

$$\begin{cases} \Delta \varepsilon_1^{ps} = \lambda^s \\ \Delta \varepsilon_2^{ps} = 0 \\ \Delta \varepsilon_3^{ps} = -\lambda^s N_\psi \end{cases} \quad (8)$$

Substitute the Eq. (8) into Eq. (1), correction equation of shear failure stress can be obtained,

$$\begin{cases} \sigma_1^N = \sigma_1^I - \lambda^s (\alpha_1 - \alpha_2 N_\psi) \\ \sigma_2^N = \sigma_2^I - \alpha_2 \lambda^s (1 - N_\psi) \\ \sigma_3^N = \sigma_3^I - \lambda^s (\alpha_2 - \alpha_1 N_\psi) \end{cases} \quad (9)$$

where, the superscripts N and I denote the new and old stress states of elements, respectively. In the same way, stress correction equation of tensile failure can be obtained,

$$\begin{cases} \sigma_1^N = \sigma_1^I - \lambda^t \alpha_2 \\ \sigma_2^N = \sigma_2^I - \lambda^t \alpha_2 \\ \sigma_3^N = \sigma_3^I - \lambda^t \alpha_1 \end{cases} \quad (10)$$

3.3. Physical and mechanical parameters of each stratum

As for the strain-softening model in Fig. 5, the rock mechanical parameters may soften or harden during the post-peak softening stage. The accurate variation of rock strength parameters is the basis for the correctness of the numerical simulation results. This research is focused on the determination of cohesion and internal friction angle. Tensile strength can be estimated based on compressive strength (Diederichs, 2007).

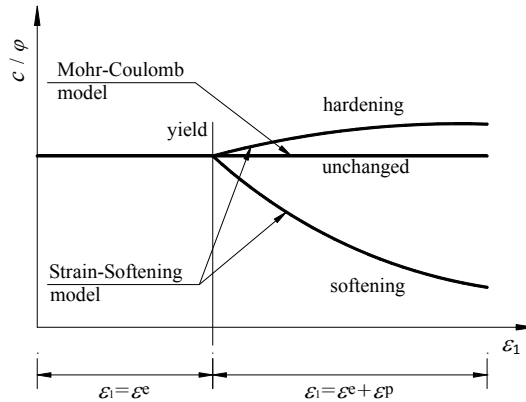


Fig. 5. Change of mechanical parameters in the Mohr-Coulomb model and strain softening model after yielding

In order to obtain the physical and mechanical parameters of some strata in the model in Fig. 3, drilling core for samples, mudstone, fine sandstone, Ordovician limestone) was conducted on site and the common triaxial compression test of 20 MPa, corresponding to the in-situ stress level, was carried out using MTS815 test machine of state key laboratory for geomechanics & deep underground engineering, China University of Mining and Technology in China. The complete stress-strain curves of mudstone, sandstone and limestone are shown in Fig. 6.

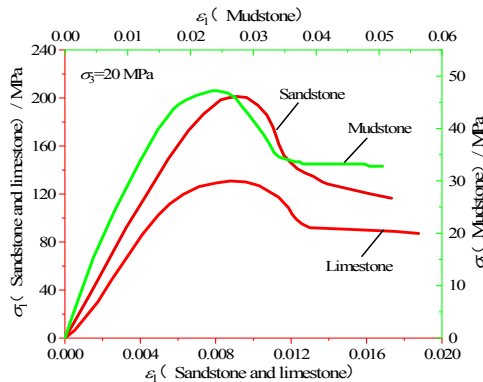


Fig. 6. Stress-strain curves of mudstone, sandstone and limestone under triaxial compression with a confining pressure of 20 MPa

Fig. 7 shows a representative model of cohesion weakening and friction strengthening (CWFS) for rock proposed by Hajiabdolmajid et al. (2002). Points A, B and C on the stress-strain curve indicate the micro-crack generation, the peak strength and the beginning of the residual strength, respectively, while A', B' and C' are the corresponding strains for the three points. The stress-strain curve can be roughly divided into three stages, pre-peak elasticity OA and elastic-plastic stage AB, post-peak softening stage BC, and residual strength stage after C point. Moreover, the axial stress is undertaken by two parts, the cohesive strength and the internal friction strength. The cohesive strength can be activated by the initial loading while the friction strength begins to be mobilized by the generation of micro-cracks in Fig. 7(b) and 7(c), respectively. The cohesive strength and the friction strength can be extracted from the stress-strain curve in Fig. 7(a). Before the residual deformation stage, with the increase of axial strain, the cohesive strength increases first and then decreases, while the friction strength increases continuously. The changes of the cohesive strength and friction strength in the softening phase are shown in the curves in the dotted box 1 of Fig. 7(b) and the dotted box 2 of Fig. 7(c), respectively. The downward trend of post-peak curve is very similar to the quadratic function curve under the relatively high confining pressure, especially for the gentle post-peak failure.

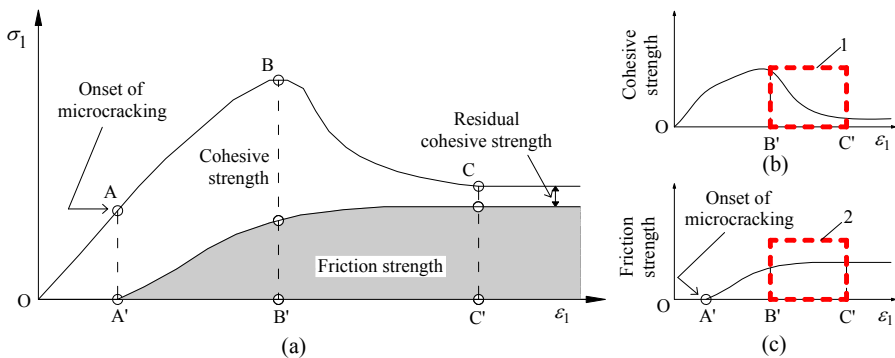


Fig. 7. Cohesion weakening and friction strengthening model (after Hajiabdolmajid et al., 2002)

Because the activation and mobilization of cohesion and internal friction angle are responded to the increment of actual external load or strain, the effective cohesion and internal friction angle in softening stage have a function relationship with axial strain (Li et al., 2011), and then, substituted effective cohesion and internal friction angle into the M-C strength criterion. It is general that the stress-strain state at the points in the softening phase meets with M-C criterion (Zhang et al., 2008). In this way, the variation of effective cohesion and internal friction angle of the mud rock, sandstone, limestone in post-peak softening stage can be obtained by fitting, as shown in Fig. 8.

As can be seen from Fig. 8, with the increase of strain, the effective cohesions of mudstone, sandstone and limestone decrease with an increasing rate, while the effective internal friction angles increase with a decreasing rate in the softening stage. Therefore, the variation of the cohesion and internal friction angle of mudstone, sandstone and limestone after the peak can be input into FLAC^{3D} software according to piecewise linear function, the self-defined softening model can be realized in this way. Compared with mudstone, sandstone and limestone, and combined with the relative geological data (to determine the reduction coefficient) of Huainan mining area (Jiang,

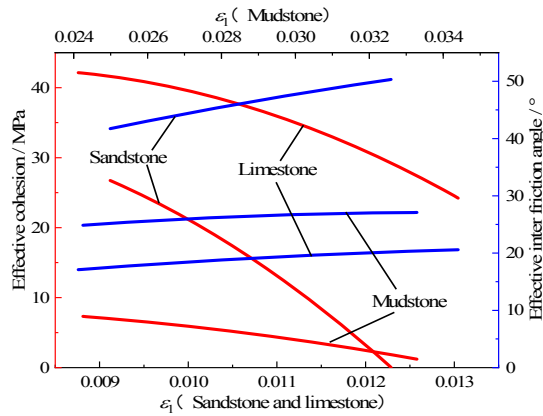


Fig. 8. Variation of effective cohesion and effective internal friction angle of mudstone, sandstone and limestone in the softening phase

2016), the approximate parameters of other rock formations can be determined by difference method. The physical and mechanical parameters of each rock strata inputted in the numerical model are shown in table 1. The residual strength parameters are considered to be unchanged.

TABLE 1

Physical and mechanical parameters of each rock strata in numerical model

Rock strata	Density /g/cm ³	Elastic modulus /GPa	Poisson's ratio	Cohesion /MPa	Internal friction angle /°	Tensile strength /MPa
Fine sandstone	2.75	2.0	0.23	2.8	34	3.0
Sandy mudstone	2.56	1.8	0.24	2.5	28	2.2
13-2 coal	2.40	1.5	0.20	1.2	22	1.8
Mudstone 1,2	2.68	0.8	0.22	1.8	22	2.0
13-1 coal	2.40	1.8	0.22	1.2	24	1.5
Siltstone	2.65	1.6	0.25	2.3	26	2.5
Medium granite Sandstone	2.70	2.2	0.21	2.5	30	3.0
Ordovician limestone	2.60	1.6	0.23	3.0	20	3.0
Fault	2.0	0.6	0.20	0.6	15	0.5

4. Analysis of strata pressure and axial bolt load based on simulation results

4.1. Distribution of the abutment pressure in front of the working face

During the mining process, the abutment pressure was accumulated in the rock mass in front of the working face. At the middle section of the panel along the strike direction, the simulated

results of the abutment pressure are collected from the working face towards the fault. As the coal mining advances, the temporal and spatial variation of the abutment pressure is shown in Fig. 9. The abscissa in Fig. 9 is consistent with the Y-coordinate of the model (see Fig. 3).

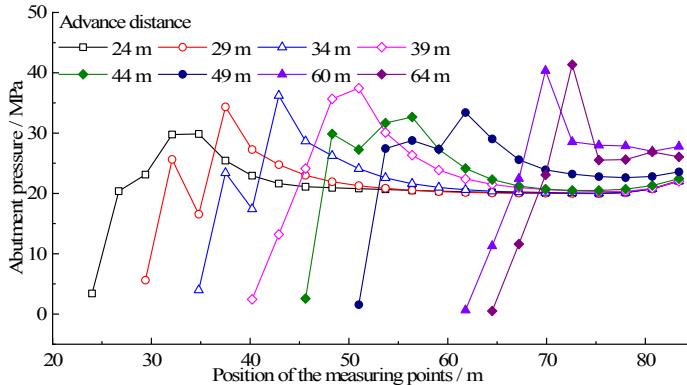


Fig. 9. Abutment Pressure in the middle section of panel along the strike direction

When the working face is advanced 24 m, the abutment pressure increases first and then decreases within the distance of 20 m before working face. The maximum abutment pressure is present at the position of 34 m, that is, about 10 m far from the working face. At the peak position, the abutment pressure is increased from 20 MPa to 30 MPa. The stress concentration coefficient there is 1.5. Outside the range of 20 m, the abutment pressure almost keeps stable at 20 MPa. When the working face is continuously advanced, the abutment pressure shows a very similar distribution like before and the concentration coefficients of the maximum abutment pressure are all between 1.5 and 2.0. Specifically, the maximum abutment pressure is about 30 MPa when the working face is advanced 24 m and 44 m. The maximum abutment pressure is increased to about 34 MPa, 36 MPa and 37 MPa correspondingly when the working face is advanced 29 m, 34 m and 39 m, respectively.

When the working face is advanced 24 m and 44 m, the first roof weighting and second weighting occurred at that time (to be described in the following section 4.3). The collapsed roof strata fell down to the floor and the floor supported some parts of the gravity of overburden strata. Therefore, the front abutment pressure is relatively smaller than that during coal normal advancing. When the face is advanced 29 m, 34 m and 39 m, the roof overlying on the gob is under a condition between the first weighting and the second weighting. That is to say, the basic roof does not break off but the hanging range of the roof increases gradually, which results in the increase of the gravity of overburden strata exerted on the rock mass in front of the working face. The front abutment pressure is increased correspondingly.

When the working face is advanced 60 m and 64 m, the stress concentration coefficient is about 2.0. This is because the working face starts to be influenced by the fault when the face approaches to 60 m. The existence of the fault destroys the continuity of the rock strata, which causes that the support effect of rock mass in front of the face cannot move forward through the fault effectively. So the decrease of supporting range of rock mass leads to the increase of concentration coefficient of the front abutment pressure.

4.2. Detection of roadway convergence between roof and floor

The measurement points of roadway convergence between roof and floor is chosen at A and B in Fig. 2. Along the direction of coal advancing, the convergence of the entry (pointed by an arrow in Fig. 3) at different positions starting from the working face was collected in the simulation. One representative example of rock strata movement at a certain coal advancement is shown in Fig. 10 and the convergence results of the entry at different advance distances are shown in Fig. 11. The abscissa in Fig. 11 is also consistent with the Y-coordinate of the model.

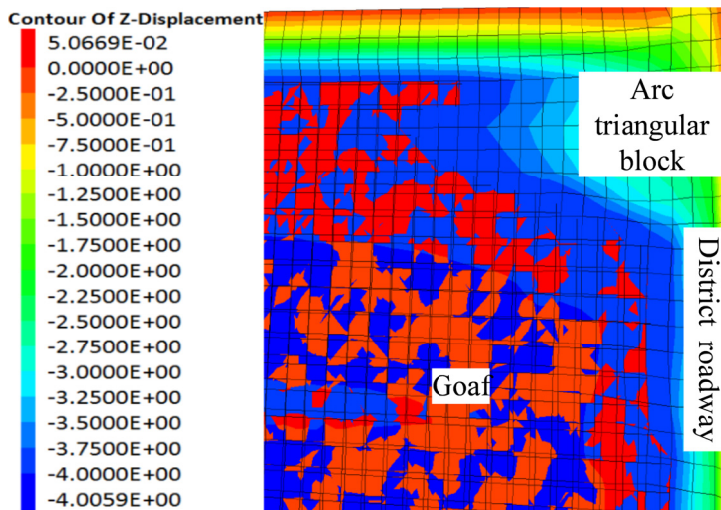


Fig. 10. One representative example of rock strata movement

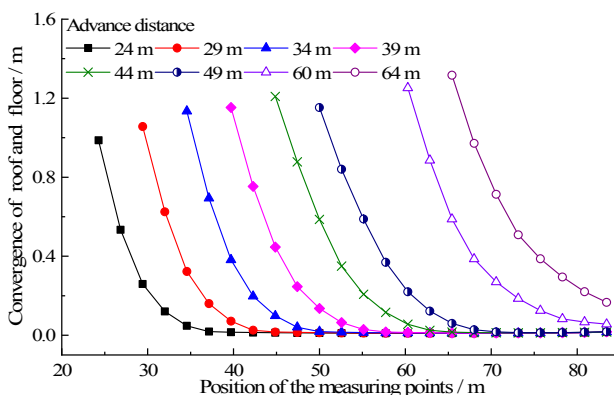


Fig. 11. Roadway convergent between roof and floor in front of the working face

It can be seen from Fig. 11 that when the working face is advanced 24 m, the maximum convergence is gained at the face wall and the value is about 1.0 m. The roadway convergence

is gradually decreased within the range of about 15 m ahead the working face. The convergence outside the range of 15 m is almost negligible. Similarly, in the subsequent coal advancing, the spatial distribution of roadway convergence has a similar change trend. In particular, before the working face is advanced 49 m, the maximum convergence is about 1.10 m. Therefore, it can be concluded that the normal range of roadway convergence before the working face is about 15 m. When the working face is advanced 60 m and 64 m, the range of heavy convergence is enlarged to about 24 m, reaching to the position of the fault correspondingly. The maximum convergence is increased to 1.30 m. It can be seen from the section of 4.1 that the working face is influenced by the fault when advanced 60 m. The existence of the fault increases the front abutment pressure, leading to the increase of the roadway convergence.

4.3. Temporal and spatial distribution of axial bolt load

The measurement points of axial bolt load are selected at the point (A) of the middle roof in each roadway section, as shown in Fig. 2. After the accomplishment of the calculation at each excavation step, the data of all the measurement points at different roadway sections along the advance direction are collected. And then the calculation of the next excavation step can be carried out. Repeat to do that model calculation and the collection of axial bolt loads until the coal seam of the foot wall is fully mined out.

Fig. 12 shows the simulation results of the axial load of roof bolts with coal advancing. The abscissa in Fig. 12 is consistent with the Y-coordinate of the model. When the working face is advanced at different positions, axial bolt loads at different measurement points in the full range of the fault footwall were collected.

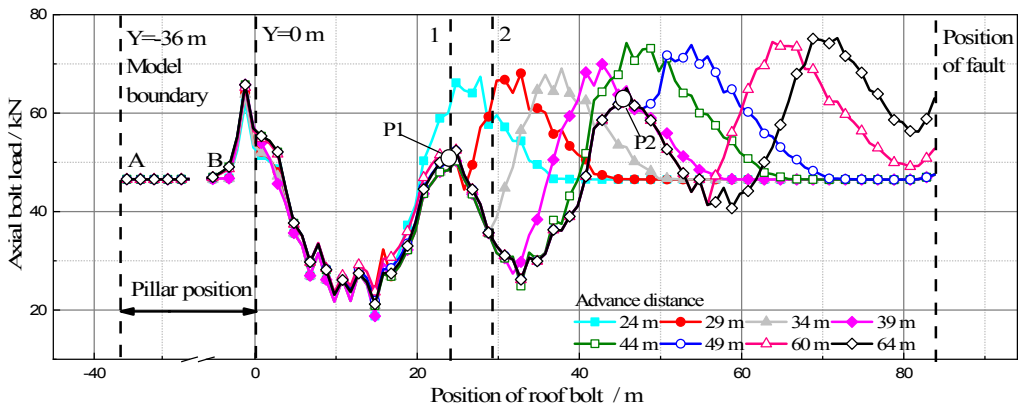


Fig. 12. Spatial and temporal distribution of the axial load of roof bolts with the mining advance

Under the condition that a coal safety pillar 36 m wide left behind the face (see Fig. 3) and due to the restriction of the model boundary, axial bolt loads in the range of 0 to 32 m (point A to B in Fig. 12) almost don't change, which might be slightly influenced by mining disturbance during the coal advancing 19 m. When the working face is advanced from 0 m to 19 m, the roof of the mined out area has not yet broken and has a high self-bearing capacity (Li et al., 2014). In

this stage, the rock deformation and the change of axial bolt load are relatively small. When the working face is advanced about 24 m (dotted line 1 in Fig. 12), the basic roof is broken off at the first time. The axial bolt load in the range from 24 m to 39 m increases first and then decreases. At the position of 28 m, it reaches a peak value. The axial bolt load is increased by about 43% (from 47 kN to 67 kN) at the peak point. While the axial bolt load tends to be stable outside 39 m, that is, the advanced timbering support can be set as a range of about 15 m (from 24 m to 39 m). When the working face is advanced about 29 m (dotted line 2 in Fig. 12), the axial bolt load reaches the peak value at 33 m and keeps stable outside 44 m, the range of advanced support is also about 15 m (from 29 m to 44 m). Compared to the peak position of axial bolt load when advanced 24 m, the peak position of the axial bolt load jumps forward about 5 m (from 28 m to 33 m). When the face is advanced to other positions, the variation of axial bolt load reappeared, in accordance with the above law.

When the face is advanced 24 m and 44 m, the first weighting and second weighting occur correspondingly, the weighting process can be also clearly reflected in the temporal and spatial distribution of axial bolt load. For example, when the working face is advanced 24 m, it is found that the axial load of the bolt decreases sharply at the position of 24 m (see point P1 in Fig. 12). This is because the measurement point of the axial bolt load at 24 m is located near the coal wall of the face and the rock mass of the roadway roof at that position is heavily fractured under the severe influence of first weighting. As a result, the axial bolt load is decreased at 24 m and the location of the peak value of the axial bolt load jumps forwards simultaneously.

Similarly, after the working face is advanced 44 m, the axial bolt load decreases drastically (see point P2 in Fig. 12) and the location of the peak value of the axial bolt load jumps forwards, which corresponds to the second weighting. The third weighting occurs when the working face is advanced 64 m. From that moment, the axial bolt load is not collected. From the above analysis, it can be seen that the periodic weighting distance of rock strata above the stope is about 20 m. When the working face is advanced 60 m, under the serious influence of the fault located at 84 m, the range of heavy mining disturbance or advanced timbering support is increased to about 24 m (from 60 m to 84 m, see Fig. 12). Compared with that when the face is advanced 24 m and 49 m, the range increment is about 9 m (from 15 m to 24 m), which manifests that the fault was activated at the time of coal advance distance 60 m.

4.4. Change mechanism of axial load of single bolt

The first weighting occurs when the working face is advanced 24 m. The change of the axial bolt load and the deformation of surrounding rock at the roadway section of $Y = 24.8$ m are collected. The simulated results of the axial bolt load and the deformation of the surrounding rock along the bolt body is shown in Fig. 13.

The working face is advanced from 0 m to 18 m, corresponding to the process of the calculation time steps from A to B (see Fig. 13). The overlying strata of the stope remain stable. The deformation of rock mass along the bolt body is negligible and the axial bolt load keeps basically unchangeable, about 47 kN. When the working face is advanced from 18 m to 24 m, the calculation steps are between point B and C in Fig. 13. At this stage of coal advancing, the deformation of the rock mass along the bolt body is relatively small and the axial bolt load basically keeps unchanged. To sum up, the overlying roof strata is still relatively stable from the advance distance from 18 m to 24 m.

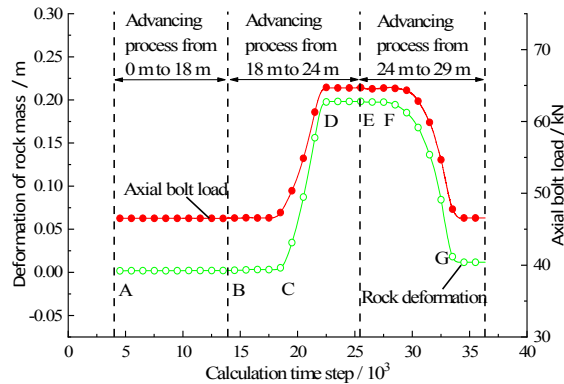


Fig. 13. Change of axial bolt load with the deformation of surrounding rock at $Y = 24.8$ m

When the calculation steps are from point C to point D, the deformation of the rock mass is increased from 0 m to about 0.2 m. Correspondingly, the axial bolt load is increased from about 47 kN to about 67 kN. The calculation steps between D and E are the convergence process of the numerical calculation, thus the rock deformation and the axial bolt load do not change. During coal advancing from 24 m to 29 m, the deformation of the rock mass and the axial bolt load are basically the same as those when the calculation steps are between E and F. The deformation of the rock mass starts to decrease at the point F and it decreases to about 0.01 m at the point G, and the axial bolt load decreases from 65 kN to about 48 kN. This is because that the coal mass at the left side of roadway at the $Y = 24.8$ m has been mined, thus the roadway roof at that location loses the support of the coal wall, so as to rotate and sink. During this process, the surrounding rock is gradually damaged, and an opposite slip occurs between the bolt body and rock mass, which makes the bolt support lose efficacy (Ding et al., 2017). The axial bolt load is consequently reduced. After the point G, the deformation of rock mass and the axial bolt load are basically the same as those in the convergence process of calculation steps.

According to the above analysis, it can be seen that the axial bolt load has a closely related with the deformation of the rock mass along the bolt body. When the deformation of the rock mass increases, the axial load of the bolt increases, and vice versa.

4.5. Variation of axial bolt load in front of or at the rear of the coal wall of the face

According to the actual situation, the bolt simulated is set as the pre-stressed bolt. Each bolt is divided into 10 segments along its length. The six segments closed to the bolt-head are the free sections while the four segments near the bolt-end are the anchorage sections. The bolt transmits the tension from the bolt-head to the anchorage zone through the free sections so as to achieve the supporting function. Since no friction exists between the free sections and the rock mass, the axial load of each free segment of the bolt are equivalent, as shown in Fig. 14.

After the mining out of the coal seam, the left side of the roadway is connected with the working face. The right side of the roadway is in a suspended state, as shown in Fig. 14(b). When the roof weighting occurs, the collapse of the main roof will inevitably drive the strata to fall

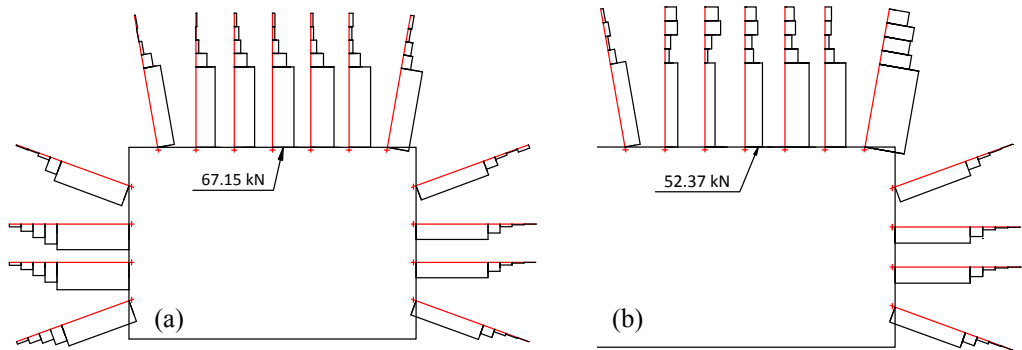


Fig. 14. Distribution of axial bolt load at the section of $Y = 24.8$ m before and after the working face;
 (a) Distribution of axial bolt load at the section of $Y = 24.8$ m in front of working face,
 (b) Distribution of axial bolt load at the section of $Y = 24.8$ m at the rear of working face

down. In order to study the change of the axial bolt loads in front of or at the rear of working face, based on the study of section 4.3, the roof bolts at the section of $Y = 24.8$ m are again selected to do further analysis. For the roof bolts at the $Y = 24.8$ m cross section, the results of the axial bolt loads in front of or at the rear of the coal wall are respectively collected when the working face is advanced at 60 m and 80 m, as shown in Fig. 14.

According to Fig. 14(a), when the working face is advanced to 24 m, the axial load distribution of the free segments of the roof bolts is relatively homogeneous at the cross section of $Y = 24.8$ m and the axial load is about 67 kN. In the anchorage section, the axial load of each segment decreases in turn along the bolt-end direction. It is obtained from section 4.3 that the first weighting occurs at the face to 24 m. The rock mass at the location of $Y = 24.8$ m is greatly deformed under the driving effect of the collapse and the subsidence of the stope roof, so the axial bolt load increases accordingly. According to that the axial load of the bolt is positively correlated with the deformation of the surrounding rock (see section 4.4), the deformation of the rock mass gradually decreases from the surface to the inner part of the roadway (H.Q. Zhang et al., 2015; Zhang et al., 2010), which is the main reason for the decrease of the axial bolt load along the bolt-end direction. During the advancing process from 24 m to 44 m, the roof at the section of $Y = 24.8$ m has been rotated and collapsed. When the bolt reaches a stable state, the axial loads of each free segment of the roof bolts have much difference. Except that the axial load of the bolt on the right corner is significantly increased, the axial load of bolts at other positions has a certain degree reduction. The axial load distribution of the anchorage section of the same bolt also changes. The anchoring force in the two segments closed to the bolt-end section increases while the anchoring force of the other two sections reduces as shown in Fig. 14(b). Due to the support of the right side of the roadway, the roadway roof rotates along the upper-right corner, which would result in serious tensile deformation of the rock mass at the corner and the axial bolt load increases significantly. For the other bolts at other positions in the same roadway section, the driving effect of the collapsed roof at the first weighting becomes weakened in the rock rotation and sinking process, which leads to the reduction of rock deformation (see Fig. 13) and axial load along the bolt at the free section. During the roof sinking process, the heavier damage of the rock mass closer to the surface of the roadway causes a more reduction of the anchoring force at the anchorage section (Wu et al., 2013). When the anchoring force adjacent to the free

section is difficult to balance the axial tension, the anchoring force will move towards the inner part, as shown in Fig. 14(b).

5. Comparison of simulation results with field measurement results of axial bolt load

The distribution of front abutment pressure, roadway convergence between roof and floor, the spatial and temporal distribution of axial bolt load and its change mechanism have been studied systematically in the above numerical simulation. The above research is of great significance for the coal safe production, but it is not clear whether the above simulation results can accurately reflect those in actual situation. Therefore, the correctness of the simulation results will be verified by field measurement results of axial bolt loads and strata pressure behavior.

5.1. Detection scheme for the axial load of roadway bolts in mining disturbance area

The axial bolt load is measured by a CMW3.7 nondestructive bolt detector which is a kind of non-destructive testing technology based on the principle of elastic dynamics. The schematic diagram of its non-destructive detection is in the following. Firstly, the sensor connection device is tightened on the exposed end of the bolt (see Fig. 15). A transverse vibration of the bolt is gently excited by a tapping on the connection device via a small hammer, which makes the buried bolt in rock mass play a part role of axial load testing sensor; then the bolt vibration signal is collected through a signal acquisition system. By virtue of the signal analysis system, the axial bolt load is calculated through the spectrum analysis and intelligent identification of the collected vibration signal (K. Zhang et al., 2015; Zhang et al., 2017a). The testing method and detection equipment of axial bolt load is shown in Fig. 15.

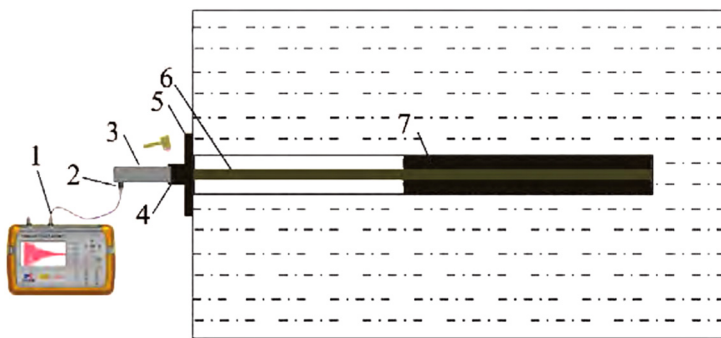


Fig. 15. Detection sketch map of axial bolt load

Compared to the bolt dynamometer, hydraulic pillow and other traditional observation methods of axial bolt load, this instrument does not require fixed-point installation of sensor or detection equipment. It can test the axial bolt load randomly with no damage to rock bolt support

structure. At the same time, this instrument has the characteristics of intrinsically safe, explosion proof, high sampling accuracy and convenient operation. A good repeatability and the measurement accuracy have been verified by the non-destructive testing calibration system and the field engineering practice (Zhang et al., 2013).

The field measurement of axial bolt load in the mining disturbance area is often conducted in the belt entry, so that it is free from any disturbance of material or equipment transportation in the tail entry. Generally speaking, the monitored region is within more than 30 m outby the face until it is beyond the severe mining disturbance area and deep into the area where the support pressure is stabilized. As is shown in Fig. 16, in the belt entry outby the face, every two or three rows of bolts was selected in one test cross section. In case the test cross section changes greatly (e.g. severe deformation or changes of shape or size), testing can be strengthened to every row; in case that the mining disturbance is comparatively slight, the testing density can be reduced accordingly. Then, the bolts in the same position of the roof and the ribs (e.g. the center bolt) are selected and numbered along the roadway axis. As the face moves forward, the test area of axial bolt load needs to move forward simultaneously and more bolts need to be selected and numbered accordingly to ensure that the test area of axial bolt load covers sufficient distance. Accordingly, the CMW3.7 nondestructive testing instrument is used to test and record the change of axial bolt load as the face advances.

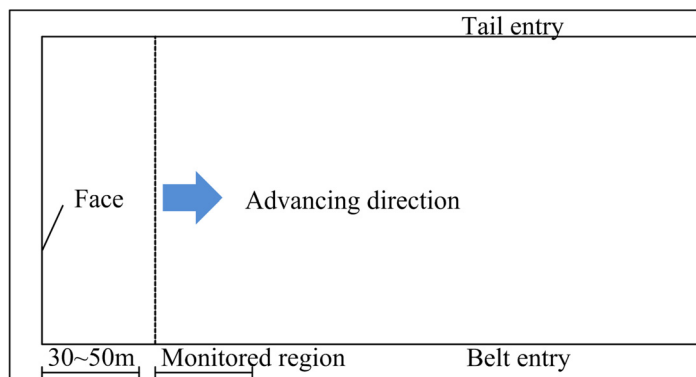


Fig. 16. Relation between the detection zone of axial bolt load and working face

5.2. Distribution of axial bolt load in front of working face

Fig. 17 shows the measured results of the axial load of the roof bolts with the advance of working face (without the influence of fault). It can be seen from Fig. 17 that with the advance of working face, the mining disturbance on the rock around the roadway is different, which induces that the axial load of the same roof bolt has been increased or decreased at different test times (time domain), and the change trend of bolt load at different positions (spatial domain) before the working face is different.

As the face advances to 36.2 m, the main roof breaks off at the first time. The test results of axial bolt load before and after the first roof weighting are shown in Fig. 18 and Fig. 19. From the two figures, it can be seen that no matter how far the face advances, the axial load of

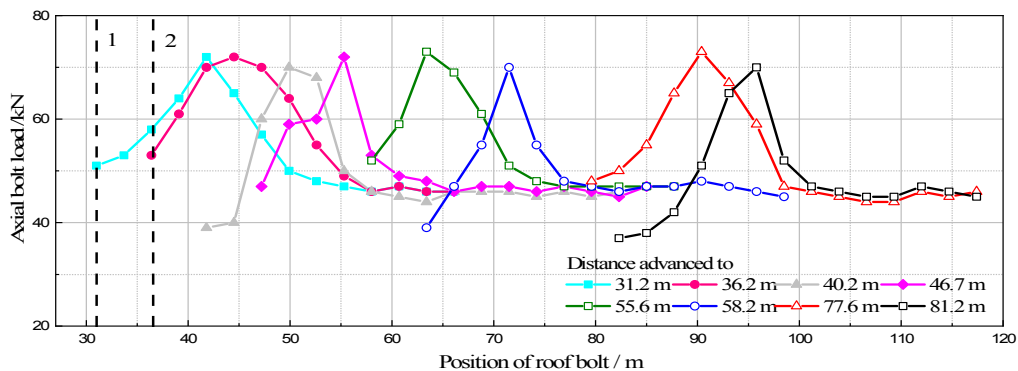


Fig. 17. Measured results of axial bolt load at different coal advance distance

roof bolts presents an overall distribution trend: increase to the peak value first and then decline gradually until it stabilizes. Within the distance of 0 m-20 m from the face, the axial load of roof bolts increases first and declines afterwards; beyond this range, the axial load of roof bolts tends to be stabilized. This indicates that the area of 20 m ahead of the face is under severe mining disturbance and the strata pressure changes drastically. At the distance of 10 m from the face, the axial bolt load reaches the peak value.

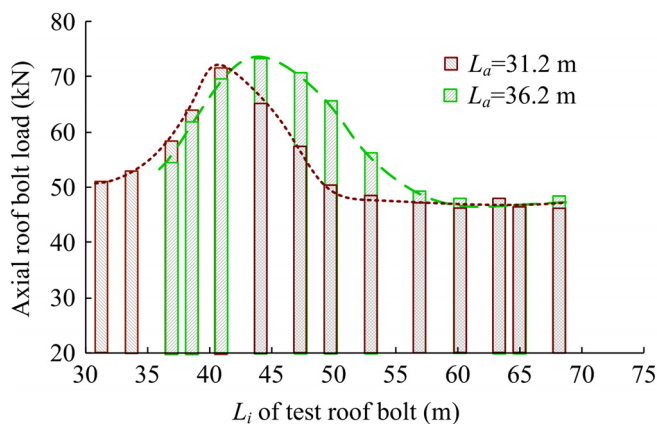


Fig. 18. Measured results of axial bolt loads before the first fracture of main roof

Before the failure of the main roof, the extreme values of axial roof bolt load increases when the face advances from 31.2 m to 36.2 m. The point of peak axial load moves forward as well (see Fig. 18). This suggests that before the failure of the main roof, the roof pressure in the coal-rock mass ahead of the face increases gradually while the peak point shifts deep into the coal-rock mass as the coal mining advances. A good accordance shows in the variation characteristics between simulated and measurement results.

The coal mass in the range of about 5 m ahead of the face enters into a plastic state when the stress of the surrounding rock reaches or exceeds its maximum bearing capacity. The strata

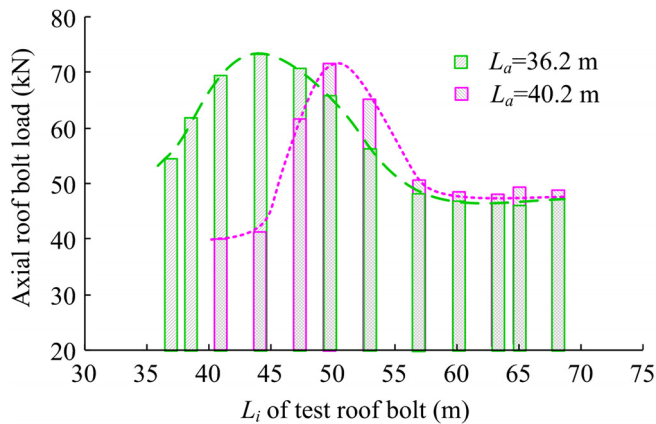


Fig. 19. Comparison of axial bolt loads before and after the first fracture of main roof

pressure is released by the fracturing of surrounding rock itself, which results in the decreasing trend of axial load of roof bolts in the range of about 5 m, as shown in Fig. 19.

In the range from 5 m to 20 m before the face, the axial load of roof bolts increases. It can be deduced from the following section of distribution of the abutment pressure in front of the working face that this is because the surrounding rock near the coal wall of the face cannot play the support function of the surrounding rock well, which induces that the front abutment pressure is propagated into the interior of the rock mass (within 5 m to 20 m).

The measured results in Fig. 19 show that violent change of the axial bolt load is within the range of about 20 m before the working face, which means the range of heavy mining disturbance is about 20 m. This result is almost consistent with the simulation results.

5.3. Weighting period of working face and dynamic response of axial bolt load

When the working face is advanced to 36.2 m, the first breaking of main roof occurs (see Fig. 19). Through the comparison and analysis of the variation curves of axial bolt load at the advance distance of 36.2 m and 40.2 m, it can be seen that the axial load of the roof bolt located within the roof breaking line is decreased drastically. The peak value of the roof bolt decreases and its position jumps forward.

In order to further illustrate the law of the dynamic response of the axial bolt load to the breaking of basic roof, Fig. 20 shows the changes of the axial load of the bolts before and after first weighting and second weighting. According to the figures, the weighting period of the basic roof is about 22 m (55.6 m to 77.6 m), which is basically in accordance with the simulation results. Combining with Fig. 19 and Fig. 20, it can be seen that the peak value of the axial bolt load has been significantly reduced after each weighting of main roof, and the location of the peak value jumps forward about 5 m to 7 m; with the continuous advance of the working face, the peak value of the axial bolt load gradually rises up again before the next weighting.

According to the above, when the working face is not affected by the fault, the temporal and spatial distribution of the axial bolt load is in good agreement with the measured results,

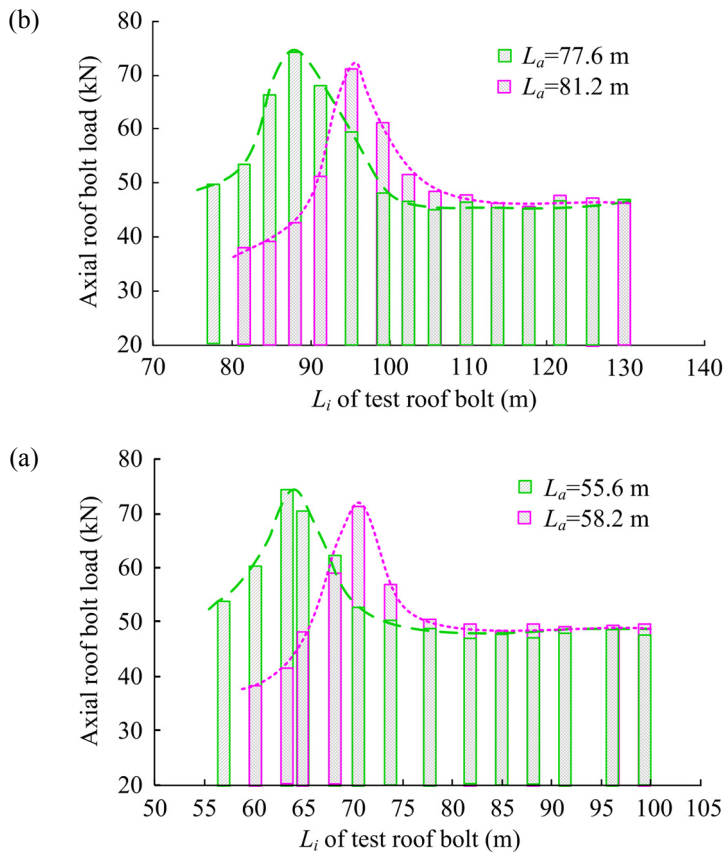


Fig. 20. First and second weighting of main roof; (a) first weighting, (b) second weighting

which demonstrates the correctness of the model setup and its simulation results. Through the simulation results, it can be predicted that when the working face is affected by the fault, the front support range of the bolt will be significantly increased.

6. Conclusions

The cohesion and internal friction angle were characterized as quadratic functions of strain and were assumed to follow with the M-C criterion after the yield of peak strength. These mechanical parameters and their variations in post-peak softening stage can be exactly ascertained through the simultaneous solution based on the data points of stress-strain curves of triaxial compression tests. Taking the influence of the fault into account, the variation of strata pressure and roadway convergence with coal advancement, the temporal and spatial distribution of axial bolt load were numerically simulated by FLAC^{3D} using the ascertained post-peak mechanical parameters according to the cohesion weakening and friction strengthening model. The change mechanism of axial load of single rock bolt as abutment pressure changes was analyzed, through

the comparison analysis with the results of axial bolt load by field measurements at a coal mine face. The research results are obtained as follows:

- 1) With the increase of strain, the effective cohesions of mudstone, sandstone and limestone decrease with an increasing rate, while the effective internal friction angles increase with a decreasing rate in the softening stage.
- 2) The simulation results of the period of the main roof weighting, the temporal and spatial distribution of axial bolt load are consistent with field measurement results, thus the correctness of the numerical model has been proved.
- 3) The front abutment pressure increases first and then decreases. After the weighting of the main roof, the abutment pressure decreases significantly. When the working face is in the middle period between two weightings, the abutment pressure will increase gradually with coal advancing. When encountered by a fault, the abutment pressure concentration coefficient will be increased greatly.
- 4) The variation of axial bolt load is closely related with the deformation of the rock mass. When the deformation of the rock mass along the bolt body increases, the axial bolt load increases, and vice versa.
- 5) The distribution of the axial load of the roof bolts along the gob is relatively uniform before the collapse of roof. After the collapse of roof, the axial load of the bolts on the side of the working face will reduce, while the other side one will increase. When the roof collapses, the heavier damage of the rock mass closer to the surface of the roadway causes the more reduction of the anchoring force on the anchorage section.
- 6) When the anchoring force adjacent to the free section is difficult to balance the axial tension, the anchoring force will move toward the interior rock mass.

Conflicts of Interest

The authors declare that they have no conflicts of interest.

Acknowledgments

Financial supports for this work, provided by the Fundamental Research Funds for the Central Universities (No. 2015XKZD06) are gratefully acknowledged.

References

- Chen Y.L., Zhang H.Q., Wu Y., Zhang G.M., Zhang L.Q., 2016. *Study on the Relationship between Mining Pressure and Axle Force of Anchor Rod*. Journal of Coal Science **41** (5), 1106-1110.
- Diederichs M.S., 2007. *The 2003 Canadian Geotechnical Colloquium: Mechanistic interpretation and practical application of damage and spalling prediction criteria for deep tunneling*. Canadian Geotechnical Journal **44** (9), 1082-1116.
- Ding S., Jing H., Chen K., Xu G.A., Meng B., 2017. *Stress evolution and support mechanism of a bolt anchored in a rock mass with a weak interlayer*. International Journal of Mining Science and Technology **27** (3), 573-580.
- Freidin A., Neverov A., Neverov S. A., 2016. *Geomechanical assessment of compound mining technology with backfilling and caving for thick flat ore bodies*. Journal of Mining Science **52** (5), 933-942.
- Hajiabdolmajid V., Kaiser P.K., Martin C.D., 2002. *Modelling brittle failure of rock*. International Journal of Rock Mechanics & Mining Sciences **39** (6), 731-741.
- He H., 2012. *Study on spatial structure evolution and induced mining mechanism of overlying strata in coal mine*. Journal of Coal Science **37** (7), 1245-1246.

- He Y.N., Zhang H.Q., 2008. *Discussion on theory and practice of partitioning of deep surrounding rock*. Chinese Journal of Rock Mechanics and Engineering **20** (11), 2369-2375.
- Itasca Consulting Group, Inc., 2012. *Fast Language Analysis of continue in 3 dimensions, version 5.0, user's manual*. Itasca Consulting Group, Inc..
- Jiang L., 2016. *Research on the law of surrounding rock movement and occurrence of underground pressure in 1272 (3) large mining height face in Dingji Mine*. Anhui University of Science and Technology.
- Li W.T., Li S.C., Feng X.D., Li S.C., Yuan C., 2011. *Study on post-strain softening mechanical behavior of rock based on Mohr-Coulomb criterion*. Chinese Journal of Rock Mechanics and Engineering **30** (7), 1460-1466.
- Li W.T., Wang Q., Li S.C., Wang D.C., Huang F.C., Zuo J.Z., 2014. *Deformation and Failure Mechanism and Control of Surrounding Rock in Deep Roof Coal Seam*. Journal of Coal Science **39** (1), 47-56.
- Liu S.H., 2016. *Comparison and Application of Axial Force Loss of Bolt under Blasting Vibration in FLAC3D*. Acta Coal Science **41** (11), 2721-2733.
- Meng S., 2009. *Development of FLAC3D Preprocessing Program and Its Engineering Application*. Anhui University of Science and Technology.
- Qian M.G., Shi P.W., Xu J.L., 2010. *Mine pressure and rock formation control*. China University of Mining and Technology Press, Xuzhou, China.
- Rezae M., 2016. *Development of an intelligent model to estimate the height of caving-fracturing zone over the longwall gobs*, Neural Computing & Applications, 1-14.
- Su H.J., Jing H.W., Zhao H.H., Yu L.Y., Wang Y.C., 2017. *Strength degradation and anchoring behavior of rock mass in the fault fracture zone*. Environmental Earth Sciences **76** (4), 179.
- Tao Z.G., Zhao F., Wang H.J., Zhang H.J., Peng Y.Y., 2016. *Innovative constant resistance large deformation bolt for rock support in high stressed rock mass*. Arabian Journal of Geosciences **10** (15), 341.
- Tutlu Levent oğlu, Ferid Öge İbrahim, Celal Karpuz., 2015. *Relationship between pre-failure and post-failure mechanical properties of rock material of different origin*. Rock Mechanics & Rock Engineering **48** (1), 121-141.
- Wu Y.P., Zhai J., Xie P.S., Wu X.M., Zhuo Q.S., 2013. *Study on looseness of roadway surrounding rock based on ground penetrating radar detection technology*. Coal Science and Technology **41** (3), 32-34.
- Xu C., Yuan L., Cheng Y.P., Wang K., Zhou A.T., Shu L.Y., 2016. *Square-form structure failure model of mining-affected hard rock strata: theoretical derivation, application and verification*. Environmental Earth Sciences **75** (16), 1180.
- Xu T., Yang T.H., Chen C.F., Liu H.L., Yu Q.L., 2015. *Mining induced strata movement and roof behavior in underground coal mine*, Geomechanics and Geophysics for Geo-Energy and Geo-Resources **1** (3-4), 79-89.
- Zhang F., Sheng Q., Zhu Z.Q., Zhang T.H., 2008. *Study on post-peak mechanical properties and strain softening model of Three Gorges granite*. Chinese Journal of Rock Mechanics and Engineering (**S1**), 2651-2655.
- Zhang H.Q., He Y.N., Zhou J.J., Han L.J., Jiang B.S., Shao P., 2010. *Study on Variation Law of Strength of Rock Damage Process*. Journal of Rock Mechanics and Engineering **29** (S1), 3273-3279.
- Zhang H.Q., Miao X.X., Zhang G.M., Wu Y., Chen Y.L., 2017a. *Non-destructive testing and pre-warning analysis on the quality of bolt support in deep roadways of mining districts*. International Journal of Mining Science & Technology (6), 989-998.
- Zhang H.Q., Shi H., Li M., Wu Y., Chen Y.L., Zhang G.M., 2017b. *Study on stability of coal pillars in fully mechanized coal mining face based on axial force measurement of bolt*. Journal of Coal Science **42** (2), 429-435.
- Zhang H.Q., Tannant D.D., Jing H.W., Nunoo S., Niu S.J., Wang S.Y., 2015. *Evolution of cohesion and friction angle during microfracture accumulation in rock*. Natural Hazards **77** (1), 497-510.
- Zhang K., Zhang G.M., Hou R.B., Wu Y., Zhou H.Q., 2015. *Stress Evolution in Roadway Rock Bolts During Mining in a Fully Mechanized Longwall Face, and an Evaluation of Rock Bolt Support Design*. Rock Mechanics & Rock Engineering **48** (1), 333-344.
- Zhang K., Wu Y., Zhou Y.J., Xue D.C., 2013. *Development and application of non-destructive testing technology for non - full Length bonded bolt in coal mine*. China University of Mining and Technology Press, Xuzhou, China.
- Zhang M., Shimada H., Sasaoka T., Matsui K., Dou L., 2014. *Evolution and effect of the stress concentration and rock failure in the deep multi-seam coal mining*. Environmental Earth Sciences **72** (3), 629-643.
- Zhang N.B., Liu C.Y., Yang P.J., 2016. *Flow of top coal and roof rock and loss of top coal in fully mechanized top coal caving mining of extra thick coal seams*. Arabian Journal of Geosciences **9** (6), 1-9.
- Zhou M., 2016. *Non-destructive testing of axial force of roadway in mining roadway*. Coal Mine Safety **47** (3), 212-214.